

# Research and Application of Discrete Adjoint Optimization based on Unstructured Grid

B. Li, J. Tang, H.Y. Jia, Y.B. Zhang, and Y.Q. Deng  
Corresponding author: leebin2018@icloud.com

China Aerodynamic Research and Development Center, China

**Abstract:** Based on unstructured grid, a discrete adjoint optimization framework is developed for a 3D RANS solver MFlow, while FFD technology is utilized to transform mesh for the next optimization cycle. Discrete adjoint equation is acquired directly by formula derivation method and solved through LU-SGS iteration. The convergence of LU-SGS method for adjoint equation and the simplified strategy for limiter are validated in this paper. The optimization system is successfully demonstrated for a DLR F6 wing-body transonic shape optimization design, in which 112 design variables are selected with the purpose of reducing drag. The another application is bump optimization, with the aim of increasing total pressure recovery coefficient. It shows that the efficient optimization framework has a bright application prospect for three-dimensional complex shape design.

*Keywords:* Discrete Adjoint Optimization, LU-SGS, Unstructured Grid.

## 1 Introduction

Shape is crucial for aircraft, by which aerodynamic characteristic is determined. With the development of computer and CFD technology, it is more and more valued to combine CFD and optimizing methods, which are utilized to aerodynamic shape optimization. Combined with optimization methods, adjoint optimization method is utilized by solving the adjoint equations of flowfield to obtain sensitive derivative of the objective function indirectly. Because solving adjoint equation doesn't depend on the number of design variables, there is no relationship between the calculation amount of iterative optimization and the number of design variables. This is the most significant advantage of adjoint optimization, avoiding the problem of a great amount of calculation, and making it become viable that masses of variable are used in engineering design optimization problems.

It is very convenient to distribute grids in complex shape using unstructured grid which has good flexibility, but doesn't have the limit of nodes, thus, the unstructured grid is widely used in the application of numerical simulation. Based on unstructured grid, discrete adjoint optimization method is developed widely.

Elliott and Peraire solved the laminar flow optimization using 3D unstructured grid<sup>[1]</sup>. Nielsen and Anderson adopted Reynolds Averaged Navier-Stokes equation, combining one-equation turbulence model, to develop a parallel discrete adjoint optimization method, by which the optimization of multi-element airfoil and ONREA M6 was finished<sup>[2-3]</sup>. Nielsen and Kleb continuously implemented complex variables to discrete adjoint operators<sup>[4]</sup>. Mavriplis developed multigrid technology to the adjoint solver to speedup the convergence<sup>[5-6]</sup>. Brezillon and Dwight added the adjoint optimization model into TAU, which was developed by

DLR<sup>[7][8]</sup>. Other adjoint solvers were developed independently based on unstructured grid, such as Carpentieri and Koren<sup>[9]</sup>, Giles and Duta<sup>[10]</sup>, Guan<sup>[11]</sup>.

In this paper, we present the development of a manual-chain-based derivation discrete adjoint framework on a RANS code MFlow, which is developed to industry by China Aerodynamic Research and Development Center, for applications to aerodynamic optimization problems. The framework of the paper is organized as follows. In part 2, the MFlow solver and the developing optimization framework including Free-Form Deformation approach for mesh moving as well as the LU-SGS for discrete adjoint solver are presented. Optimization results on DLR F6 wing-body transonic shape and bump are presented in part 3. Conclusions and directions for future activities are outlined in part 4.

## 2 Optimization Framework

### 2.1 Industry Aerodynamic Solver MFlow

Autonomous numerical simulation solver MFlow is specifically developed to predict the subsonic and supersonic flowfields of complex aircraft for aerospace industry<sup>[12, 13]</sup>. The control equation is compressible Navier-Stokes equation, which is spatially discretized using the finite volume method, based on unstructured grid. The solver has many kinds of spatial format, limiter, gradient solution, boundary condition and turbulence model, which could be choose according to the problem.

Sovler MFlow participated in the 5th and the 6th AIAA CFD Drag Prediction Workshop and the 2nd AIAA CFD Hihg-Lift Prediction Workshop<sup>[14-16]</sup>. Comparing the calculation results with other CFD codes or commercial softwares, it shows that the prediction precision of Mflow Solver is excellent as well. Figure 1 and 2 give the results, shown by the organizing committee.

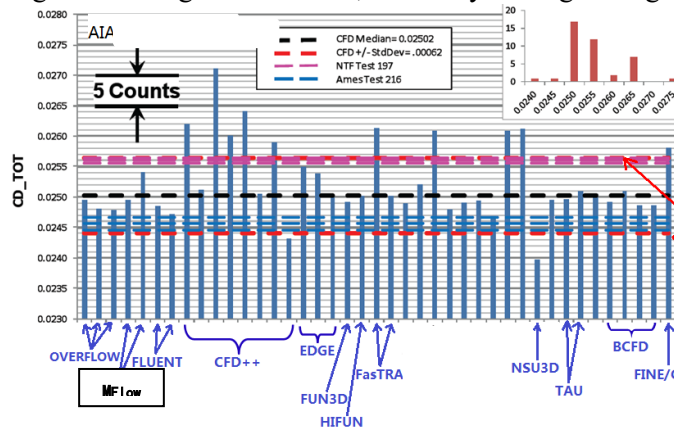


Figure 1: Result comparison from 5th DPW

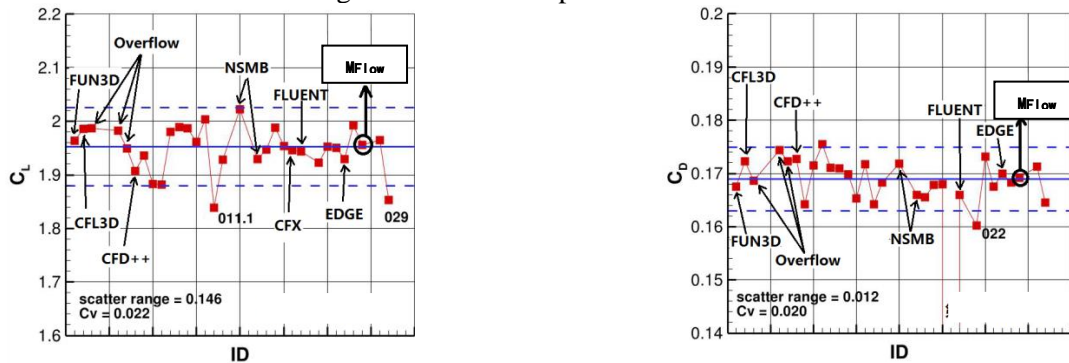


Figure 2: Result comparison from HilitPW-2

## 2.2 Discrete Adjoint Solver

As we known, discrete adjoint equation is shown as

$$\frac{\partial F}{\partial \mathbf{W}} + \Lambda^T \frac{\partial \mathbf{R}}{\partial \mathbf{W}} = 0 \text{ or } \left( \frac{\partial \mathbf{R}}{\partial \mathbf{W}} \right)^T \Lambda = - \left( \frac{\partial F}{\partial \mathbf{W}} \right)^T$$

where  $F$  is the objective function, and the vector  $\mathbf{R}$  is the residual of flow-field equation solved using MFlow while the vector  $\mathbf{W}$  is the conserved variables for mass, momentum, and energy. The vector  $\Lambda$  is Lagrange multipliers associated with the flow-field equation.

To improve the stability of solving adjoint equation, pseudo time term is added,

$$\iiint_V \frac{\partial \mathbf{A}}{\partial t} + \left( \frac{\partial \mathbf{R}}{\partial \mathbf{W}} \right)^T \mathbf{A} + \left( \frac{\partial F}{\partial \mathbf{W}} \right)^T = 0$$

The implicit Euler method is implemented and linearizing around  $\Lambda^n$

$$\left( \frac{V}{\Delta t} \mathbf{I} + \left( \frac{\partial \mathbf{R}}{\partial \mathbf{W}} \right)^T \right) \Delta \mathbf{A}^n = - \frac{\partial F}{\partial \mathbf{W}} - \left( \frac{\partial \mathbf{R}}{\partial \mathbf{W}} \right)^T \mathbf{A}^n$$

Most ways to solve the equation is to adopt PETS. In this paper, LU-SGS method is developed to solve the adjoint equation. For each cell  $i$ , cell  $j$  is defined as the adjacent cell of  $i$ . The equation above can be instead as

$$\left( \frac{V}{\Delta t} \mathbf{I} + \left( \sum_{j=1}^N \frac{\partial \mathbf{H}_{ij} \cdot \mathbf{n}_{ij}}{\partial \mathbf{W}_i} S_{ij} \right)^T \right) \Delta \mathbf{A}_i^n + \left( \sum_{j=1}^N \left( \frac{\partial \mathbf{H}_{ji} \cdot \mathbf{n}_{ji}}{\partial \mathbf{W}_i} S_{ji} \right)^T \cdot \Delta \mathbf{A}_j^n \right) = - \left( \frac{\partial F}{\partial \mathbf{W}_i} \right) - \sum_{m=1}^{Total} \left( \frac{\partial \mathbf{R}_m}{\partial \mathbf{W}_i} \right)^T \Lambda_m^n$$

Where  $\mathbf{n}_{ij}$  is an outward-pointing unit face normal from cell  $i$  to cell  $j$ .

First order assumption is used to left term,

$$\frac{\partial \mathbf{H}_{ij} \cdot \mathbf{n}_{ij}}{\partial \mathbf{W}_i} = \frac{1}{2} (\mathbf{A}_i + \lambda_{\max} \mathbf{E}), \quad \frac{\partial \mathbf{H}_{ji} \cdot \mathbf{n}_{ji}}{\partial \mathbf{W}_i} = - \frac{1}{2} (\mathbf{A}_i + \lambda_{\max} \mathbf{E})$$

The adjoint equation can be shown as follows, considering  $\sum_{j=1}^N \mathbf{A}_i S_{ij} = 0$

$$\left( \frac{V}{\Delta t} \mathbf{I} + \frac{1}{2} \left( \sum_{j=1}^N \lambda_{i\max} S_{ij} \right)^T \right) \Delta \Lambda_i^n - \frac{1}{2} \left( \sum_{j=1}^N \left( (\mathbf{A}_i + \lambda_{i\max} \mathbf{E}) S_{ji} \right)^T \cdot \Delta \Lambda_j^n \right) = - \left( \frac{\partial F}{\partial \mathbf{W}_i} \right) - \sum_{m=1}^{Total} \left( \frac{\partial \mathbf{R}_m}{\partial \mathbf{W}_i} \right)^T \Lambda_m^n$$

The LU-SGS iteration can be derived in the fixed cell form as

Forward sweep:

$$\left( \frac{V}{\Delta t} \mathbf{I} + \frac{1}{2} \left( \sum_{j=1}^N \lambda_{i\max} S_{ij} \right) \right) \Delta \mathbf{A}_i^{n,*} = \mathbf{RHS}_i + \frac{1}{2} \left( \sum_{j=1}^{LN} (\mathbf{A}_i^T + \lambda_{i\max} \mathbf{E}) S_{ji} \cdot \Delta \mathbf{A}_j^{n,*} \right)$$

Backward sweep:

$$\left( \frac{V}{\Delta t} \mathbf{I} + \frac{1}{2} \left( \sum_{j=1}^N \lambda_{i\max} S_{ij} \right) \right) \Delta \mathbf{A}_i^n = \left( \frac{V}{\Delta t} \mathbf{I} + \frac{1}{2} \left( \sum_{j=1}^N \lambda_{i\max} S_{ij} \right) \right) \Delta \mathbf{A}_i^{n,*} + \frac{1}{2} \left( \sum_{j=1}^{UN} (\mathbf{A}_i^T + \lambda_{i\max} \mathbf{E}) S_{ji} \cdot \Delta \mathbf{A}_j^n \right)$$

Where

$$\mathbf{RHS}_i = - \left( \frac{\partial F}{\partial \mathbf{W}_i} \right) - \sum_{j=1}^{NB} \left( \frac{\partial \mathbf{R}_j}{\partial \mathbf{W}_i} \right)^T \mathbf{A}_j^n$$

For  $\partial \mathbf{R} / \partial \mathbf{W}$ ,

$$\frac{\partial \mathbf{R}}{\partial \mathbf{W}} = \frac{\partial \mathbf{R}}{\partial \mathbf{Q}} \frac{\partial \mathbf{Q}}{\partial \mathbf{W}}$$

is utilized to simplify, where  $\mathbf{Q}$  is the vector of primitive variable.

Barth limiter is used for computing the residual  $\mathbf{R}$  of flow-field equation. In the adjoint solver,

the limiter is considered as a constant to avoid the complication of computing  $\partial \text{Limiter} / \partial \mathbf{Q}$ .

### 2.3 Free-Form Deformation and design variables

Free-Form Deformation (FFD)<sup>[17]</sup> is used to move mesh by transforming a hull, within which the mesh is enclosed. Moving the points which comprise the hull, can transform the surface and volume meshes, to simulate the deformation of shape. NURBS<sup>[18]</sup> is implemented in this section. The design variables are chosen as the points of the hull. Figure 3 shows the original hull and the new surface and volume mesh after moving the normal coordinates of the points in the second and third rows.

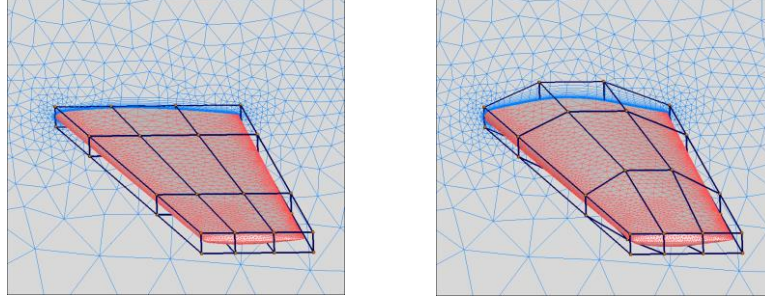


Figure 3: The movement of points of hull

### 2.4 Objective Function and Sensitivity Gradient

In the present analysis, the objective function is considered as a scalar quantity:

$$F = \omega_L \left( 1 - \frac{C_L}{C_L^*} \right)^2 + \omega_D \left( 1 - \frac{C_D}{C_D^*} \right)^2$$

Where  $C_L^*$  and  $C_D^*$  are given target lift and drag coefficients, respectively, which are integrals of the normal and tangential components of the pressure and the stress tensor over the boundary surface.  $\omega_L$  and  $\omega_D$  represent user-defined weighting factors.

The sensitivity gradient can be computed from the adjoint solutions for each design variable,

$$\frac{dF}{d\beta} = \frac{\Delta F}{\Delta\beta} + \mathbf{A}^T \frac{\Delta \mathbf{R}}{\Delta\beta}$$

Where  $\beta$  represent the design variable,  $\Delta\beta$  is the minimal variation ( $10^{-5}$ ).

Line Search method is implemented to compute the new design variable, after the sensitivity gradient is computed. Armijo-Goldstein rule is used for the step length factor, while Quasi-Newton method is utilized for the search direction.

## 3 Application

### 3.1 Convergence of Adjoint Solver

The statement of ONERA M6 at subsonic flowfield is utilized to verificate the convergence of adjoint solver. The CFL number is consistent with the one which is used in flowfield. The statement of caculation is

$$Ma_\infty = 0.8395, \alpha = 3.06$$

The history of residual for the first adjoint equation is shown in Figure 4, as well as the one for the first RANS equation, using LU-SGS as the iterator. The slope of the convergence curve is similar with the one obtained from RANS equation, It reveals that the LU-SGS method developed presently for the adjoint equation works successfully and efficiently.

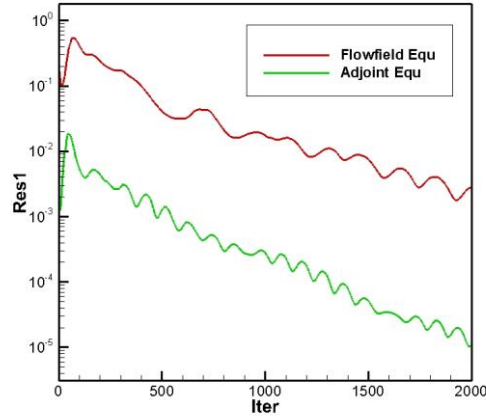


Figure 4: The history of residual for the first adjoint equation

### 3.2 Effectiveness of Simplified Derivative for Limiter

In this section, four control points on the upper surface of ONERA M6 are selected for verification. As shown in Figure 5, the points 1~4 are distributed from tip to root. The normal coordinates of the four points are selected as the design variables, and the objective functions for comparison are the lift and drag coefficients. Adjoint optimization framework is used to calculate the sensitivity gradient, which will be compared with the result from the central difference method. The statement of calculation is

$$Ma_{\infty} = 0.8395, \alpha = 3.06$$

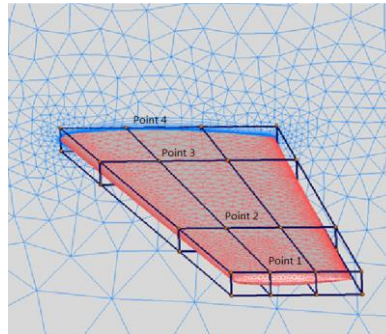


Figure 5: The points as design variables

Table 1 shows the derivatives obtained from the central difference and the adjoint method. The Barth limiter is considered as a constant for the adjoint solver. It can be shown that the simplified derivatives are basically consistent with the central difference. In this paper, the simplified strategy is implemented.

The point		finite difference	adjoint code	$\Delta\%$
$\frac{dC_L}{d\beta}$	1	1.485068E-01	1.462452E-01	-1.52%
	2	2.694556E-01	2.657428E-01	-1.38%
	3	3.694516E-01	3.568215E-01	-3.42%
	4	1.890147E-01	1.820659E-01	-3.68%
$\frac{dC_D}{d\beta}$	1	4.584685E-03	4.518409E-03	-1.45%
	2	2.441046E-02	2.415800E-02	-1.03%
	3	5.265283E-02	5.151338E-02	-2.16%
	4	2.765520E-02	2.691176E-02	-2.69%

### 3.3 DLR-F6 Configuration

The first example is a wing-body configuration DLR-F6 in transonic and turbulent flow regime. The mach number is 0.75, while the angle of attack is  $-0.1247^\circ$ . The mesh includes 1.2 million unstructured cells. In this optimization progress, geometrical constraint is considered to prevent the volume from being smaller than the minimal level. The target coefficients and weighting factors are as follows,

$$C_L^* = 0.588, \quad \omega_L = 200; \quad C_D^* = 0.02, \quad \omega_D = 1;$$

The design variables are defined as the normal coordinates of the points which enclose the wing of DLR-F6. The number of design variables is 112, as shown in Figure 6.

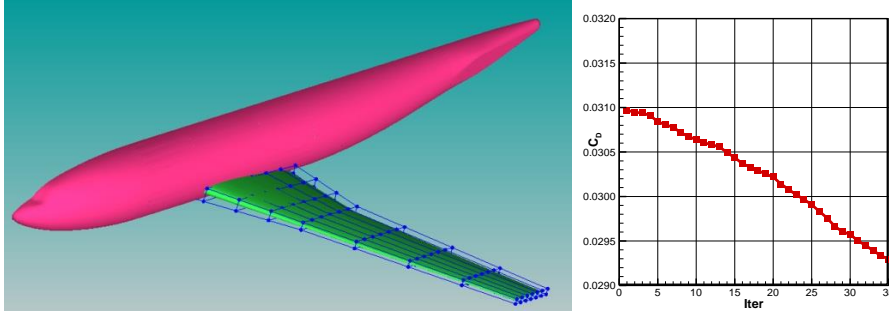


Figure 6: The 112 points for DLR-F6 Figure 7: The 112 points for DLR-F6

Figure 7 gives the variation tendency of drag coefficient. It has the trend of gradually decreasing. The fractional variation of objective function, lift and drag coefficients are shown in table 2. As we seen, the lift is basically kept during the progress, while 17 counts are reduced for drag coefficient.

	Initial	Final	$\Delta\%$
$F$	0.3072	0.2252	-26.7%
$C_L$	0.5847	0.5842	-0.09%
$C_D$	0.0310	0.0293	-17count
$K$	18.86	19.94	+5.7%

Figure 8 shows comparison of the surface pressure contour. The left part is obtained from the baseline configuration, while the right part is calculated from the optimised configuration. The shock structure closed to the wing is given in Figure 9, from which it is shown that the shock intensity is weakened by the optimization progress.

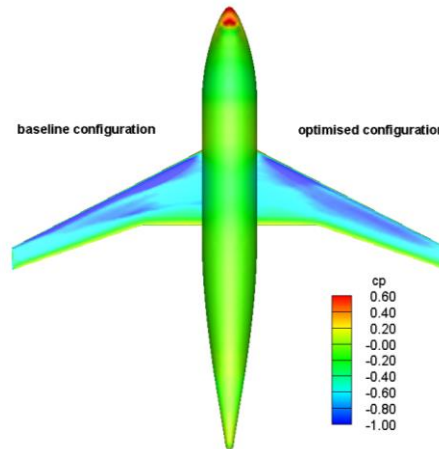


Figure 8: The 112 points for DLR-F6

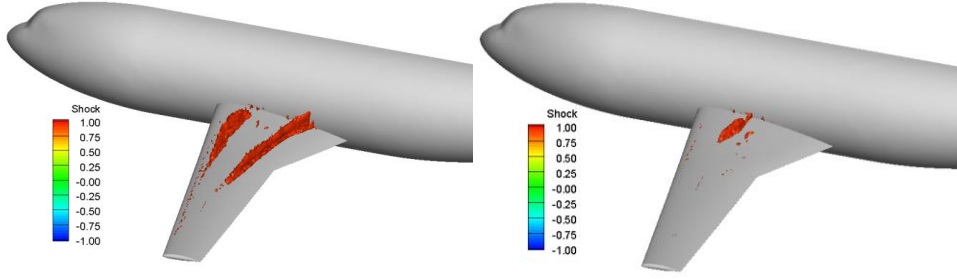


Figure 9: The 112 points for DLR-F6

### 3.4 Bump Configuration

The another application is bump optimization. The diverterless supersonic inlet (DSI) is suitable for wide range of Mach number and structure design. The shape of bump in front of the air intake of inlet makes a great influence on the flowfield at supersonic speed, which directly affects the performance of DSI inlet.

In this section, the optimization is implemented to the bump with the aim of increasing total pressure recovery coefficient  $P_{t,r}$ , while the distortion index  $D_{C60}$  is prevented from increasing.

$$\begin{cases} \max P_{t,r} = \frac{\sum_{i=1}^N S_i p_i (1 + 0.2 M_i^2)^{3.5}}{p_\infty (1 + 0.2 M_\infty^2)^{3.5} \sum_{i=1}^N S_i} \\ \text{s.t. } D_{C60} < D_{C60,0} \end{cases}$$

Where M is Mach number, and p is static pressure.  $D_{C60,0}$  represents the distortion index at the initial statement, which is shown as

$$Ma_\infty = 1.5, p_\infty = 22700 Pa, T_\infty = 216 K$$

Figure 10 is the unstructured mesh for calculation, while 18 design variables are given in Figure 11.

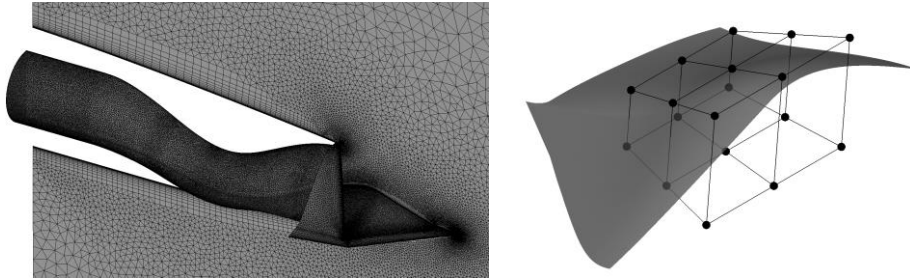


Figure 10: Surface mesh for bump optimization Figure 11: 18 design variables for bump shape After finishing the optimization, total pressure recovery coefficient increases 6%, from 0.84 to 0.89, while the distortion index decreases about 0.03. The optimization history is shown in Figure 12.

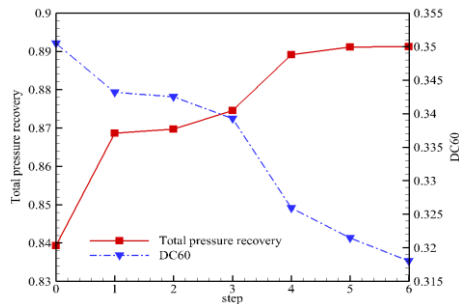


Figure 12: Optimization history of bump

Figure 13 shows the total pressure distribution of outlet. The difference of pressure distribution is weakened by the adjoint optimization framework on the plane of outlet. The normal height of bump is decreased as well, shown in Figure 14.

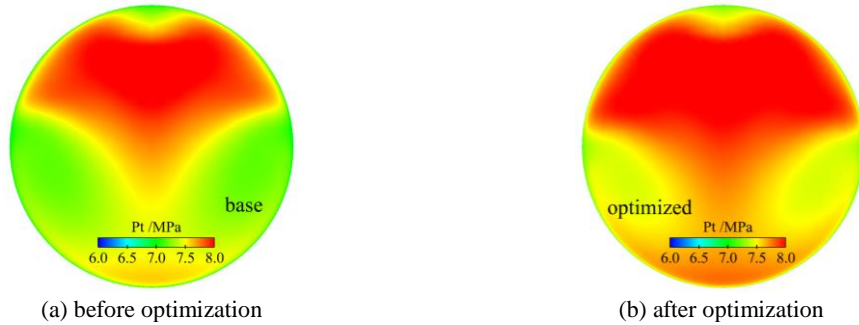


Figure 13: Optimization history of bump

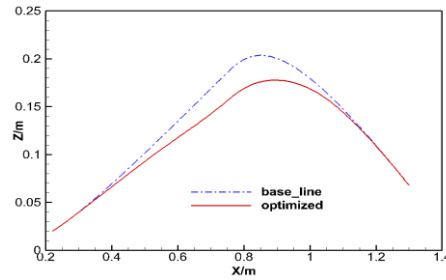


Figure 14: Comparison of bump shape on Symmetry plane before and after optimization

## 4 Conclusion and Future Work

In this paper, we present an aerodynamic optimization framework in which adjoint method and Free-Form Deformation are applied to the solver MFlow to obtain design sensitivities. A discrete adjoint solver is developed by implementing LU-SGS iterator and simplified strategy of limiterderivative, which is validated effectively by the example of ONERA M6.

The resultant discrete adjoint solver is applied to two test cases – lift-constrained drag minimization of DLR-F6 wing-body configuration in transonic turbulent flow and total pressurerecovery coefficientmaximization of a bump in supersonic flow.The results reveal that the adjoint information provided by hand discrete adjoint framework isrobustand accurate. The drag value is reduced in the first case with the lift being kept, while shock intensity closed to the wing changes. The second test caseshows that the total pressuredistribution at the plane of outlet has been changed to be average by the optimization progress. The total pressure is improved.

In the near future, we plan to apply this methology to problems with more complex geometries as well as more geometries constraint, such as the twist, thickness, angle of sweepback of wing. Furthermore, development efforts on unsteady aerodynamic optimization based on the current framework is ongoing as well.

## References

- [1] J. Elliott and J. Peraire. Practical Three-dimensional aerodynamic design and optimization using unstructured grids. *AIAA Journal*, 35(9):1479-1485, 1997.
- [2] E. J. Nielsen and W. K. Anderson. Implementation of a parallel framework for aerodynamic design optimization on unstructured meshes, *Proceedings of Parallel Computational Fluid Dynamics*:1999.
- [3] E. J. Nielsen and W. K. Anderson. Recent improvements in aerodynamic design optimization on unstructured meshes. *AIAA Journal*, 40(6):1155-1163, 2002.
- [4] E. J. Nielsen and B. Kleb. Efficient construction of discrete adjoint operators on

- unstructured grids by using complex variables. AIAA-2005-0324, 2005.
- [5] D. J. Mavriplis. Formulation and multigrid solution of the discrete adjoint for optimization problems on unstructured meshes. AIAA-2005-319, 2005.
  - [6] D. J. Mavriplis. A discrete adjoint-based approach for optimization problems on three-dimensional unstructured meshes. AIAA-2006-50, 2006.
  - [7] J. Brezillon and R. P. Dwight. Aerodynamic shape optimization using the discrete adjoint of the Navier-Stokes equations: applications towards complex 3D configurations. KATnet II Conference on Key Aerodynamic Technologies. Bremen: No.36-1, 2009.
  - [8] R. P. Dwight and J. Brezillon. Effect of various approximations of the discrete adjoint on gradient-based optimization. AIAA-2006-0690, 2006.
  - [9] G. Carpentieri and B. Koren. Development of the discrete adjoint for a 3D unstructured Euler solver. AIAA-2007-3954, 2007.
  - [10] M. B. Giles and M. C. Duta. Algorithm developments for discrete adjoint methods. AIAA Journal, 41(2):198-205, 2003.
  - [11] J. Guan. Aerodynamic shape optimization for 2D air-foil based on adjoint equations. Nanjing University of Aeronautics and Astronautics, 2011.
  - [12] P. H. Zhang and Y. B. Zhang. Gradient calculation method of unstructured mixed grids for improving drag prediction accuracy. Acta Aeronautica et Astronautica Sinica, 39(1):121415, 2018.
  - [13] J. Tang and B. Li. Large Scale Parallel Computing for Fluid Dynamics on Unstructured Grid. In 15th International Symposium on Parallel and Distributed Computing, 64-69, 2016.
  - [14] J. T. Chen and N. C. Zhou. CFD Investigations of the HiLiftPW-2 Configuration with MFlow Solver. AIAA-2014-3171, 2014.
  - [15] X. Q. Gong and J. T. Chen. The effects of turbulence model corrections on drag prediction of NASA common research model. AIAA-2014-2571, 2014.
  - [16] J. T. Chen and Y. B. Zhang. Numerical Investigations of the High-Lift Configuration with MFlow Solver, Journal of Aircraft, 52(4):1051-1062, 2015.
  - [17] E. I. Amoiralis and I. K. Nikolos. Freeform deformation versus B-spline representation in inverse airfoil design. Journal of Computing and Information Science in Engineering, 8(2):13, 2008.
  - [18] H. J. Lamousin and W. N. Waggenspack. NURBS-Based Free-Form Deformations. Computer Graphics and Applications, 14(6):59-65, 1994.